Nanoscale

PAPER

View Article Online
View Journal | View Issue

Cite this: *Nanoscale*, 2025, **17**, 15223

Efficient and color stable blue perovskite light-emitting diodes achieved *via* dual-additive phase modulation†

Peiyuan Pang, Zhipeng Zhang, Bingzhe Wang, Tao Sheng and Guichuan Xing *

Despite remarkable progress in sky-blue perovskite light-emitting diodes (PeLEDs), achieving efficient and color stable pure-blue electroluminescence remains challenging due to halide phase segregation, low-dimensional phase-induced non-radiative recombination, and defect-related losses in mixed Cl–Br quasi-two-dimensional (quasi-2D) perovskites. Here, we propose a dual-additive strategy to regulate phase distribution and manage Cl incorporation in quasi-2D perovskites for pure-blue PeLEDs. By introducing Ethylenediammonium-dichloride ($EDACl_2$) to suppress high-*n* phases and incorporate Cl for bandgap broadening, combined with NaBr to eliminate low-*n* non-radiative centers and promote small-sized nanocrystals, we optimize radiative recombination toward wide-bandgap phase distribution. This approach enables spectrally stable pure-blue electroluminescence at 474 nm without compromising photoluminescence quantum yield. Further hole-transport-layer engineering yields a peak external quantum efficiency of 4.6%, with spectral stability maintained under extreme bias up to 10.4 V. Our work provides critical insights into phase and halide management for high-performance blue PeLEDs, advancing their potential in full-color displays and lighting technologies.

Received 4th March 2025,
Accepted 22nd May 2025

DOI: 10.1039/d5nr00952a

rsc.li/nanoscale

1 Introduction

In recent years, metal halide perovskites (MHPs) have demonstrated significant potential in the fields of lighting and display, garnering widespread attention due to their superior properties, such as high photoluminescence quantum yield (PLQY), high color purity, tunable optical bandgap, high carrier mobility, low manufacturing cost, and solution processability.[1–8] The performance of PeLEDs has rapidly advanced in recent years, with reported external quantum efficiency (EQE) exceeding 20% for red, green, and blue PeLEDs,[9–24] and the highest recorded EQEs for green PeLEDs even surpassing 30%.[25–27] Despite considerable progress in the pursuit of efficiency for blue PeLEDs, high-efficiency reports are predominantly concentrated in the sky-blue region (emission peak at 480–495 nm),[28–32] while the performance of pure-blue and deep-blue PeLEDs remains relatively lagging, posing a significant obstacle to the development of next-generation full-color display devices and high-color-rendering white lighting. Therefore, there is an urgent need to construct high-performance pure-blue PeLEDs.

The construction of blue perovskite essentially involves increasing the bandgap of the perovskite material, with two common strategies being adjusting the halogen anion content and constructing perovskite structures with quantum confinement effects. For halogen adjustment, when the halogen site is changed from Br to Cl, the energies of the halide p orbitals decrease and the valence band maximum (VBM) shifts to more negative (or deeper) potentials, which results in a wider band gap.[33,34] By adjusting the Cl/Br ratio in a mix Cl–Br perovskite, seamless tuning of the emission from green to blue regions can be achieved.[35] Another strategy often implemented is the construction of quasi-2D perovskite structures, where large organic cations are introduced to adjust the orientation during perovskite crystallization, forming layered $[BX_6]^{4-}$ octahedral structures, and the bandgap of quasi-2D perovskites can be tuned by changing the thickness of the octahedral layers.[36–38] Recently, quasi-2D perovskites have shown great potential as efficient blue PeLED materials, with their unique energy funneling effect enhancing radiative recombination efficiency and avoiding defect state trapping, making them a hot candidate in blue PeLEDs. However, these two strategies also face their own difficulties. The poor solubility of chlorides in precursor solutions leads to low film coverage and high defect density in

Joint Key Laboratory of the Ministry of Education, Institute of Applied Physics and Materials Engineering, University of Macau, Macau 999078, China.
E-mail: gcxing@um.edu.mo

† Electronic supplementary information (ESI) available. See DOI: https://doi.org/10.1039/d5nr00952a

high-Cl-content perovskites, hindering the preparation of high-performance electroluminescent devices. Additionally, mixed halides perovskite are prone to ion migration under electric field driving, causing phase separation and leading to poor color stability. Quasi-2D perovskite films deposited by solution methods are usually mixtures of multiple quantum wells (MQWs) with different well widths (different octahedral layer numbers n). The multi-quantum well structure is not conducive to achieving blue electroluminescence. Due to the spontaneous energy transfer from wide-bandgap phases (low n) to narrow-bandgap phases (high n), even if a minimal amount of high n phase will lead to a red shift in luminescence. Furthermore, the large amount of organic cations introduced to construct wide-bandgap quasi-2D structures also reduces the conductivity, which is unfavorable for the preparation of high-efficiency electroluminescent devices.

Since component and structural regulation are not conflicting, the above two strategies can be used simultaneously. By introducing additives or using multiple ligand materials, the quasi-2D phase distribution can be effectively regulated, and combined with halogen regulation, the spectra can be adjusted to the desired position.[39,40] The *in situ* halide ion exchange strategy has also largely solved the problem of poor chloride solubility.[41,42] However, compared to the excellent device performance of sky-blue PeLEDs, pure-blue quasi-2D PeLEDs with mixed Cl–Br only exhibit moderate performance and still face issues of spectral stability. This is because the low-dimensional phases (n = 1, n = 2 phases) in quasi-2D perovskites guide a large amount of non-radiative recombination,[43,44] and the deep-level defects brought by Cl also reduce the radiation recombination efficiency.[45,46] Additionally, higher chlorine content makes pure-blue PeLEDs more prone to phase separation during operation.

Here, we propose a phase distribution regulation and Cl management strategy for pure-blue quasi-2D PeLEDs. First, quasi-2D sky-blue perovskite is constructed using propylammonium bromide (PABr) and phenylethylammonium bromide (PEABr) dual ligands materials, then $EDACl_2$ is introduced to inhibit the generation of high-dimensional phases in the phase distribution and to incorporate Cl, thereby blue-shifting the EL spectrum. However, the introduction of additional Cl reduces the radiation recombination rate, resulting in a decrease in PLQY. Further introduction of NaBr suppresses the low-dimensional phase of the phase distribution to eliminate non-radiative recombination centers, covers the negative effect caused by Cl, and Na^+ promotes the generation of small-sized nanocrystals, further broadening the bandgap of the perovskite. Under the combined effect of $EDACl_2$ and NaBr additives, the phase distribution of quasi-2D perovskites is significantly modified. Low-n phases that are unfavorable for radiative recombination and narrow-bandgap high-n phases are suppressed, with radiative recombination centers shifting towards the wide-bandgap n = 3 and n = 4 phases. Spectrally stable pure-blue PeLEDs are achieved without sacrificing the radiation recombination efficiency. Further optimization of the hole transport layer increases the device EQE to 4.6%, and the electroluminescence spectrum remains stable at 474 nm even under an extreme bias of 10.4 V.

2 Experimental section

2.1 Materials

NaBr (99.99%) was purchased from Aladdin. PEABr (99.5%), PABr (99.5%), $EDACl_2$ (99.5%), and poly(4-butyltriphenylamine) (poly-TPD) were purchased from Xi'an Polymer Light Technology Corporation. Poly(9-vinlycarbazole) (PVK) (M_v = 25 000–50 000), $PbBr_2$ (99.999%), CsBr (99.999%), CsCl (99.999%), DMSO (anhydrous, 99.9%), PSSNa (average molecular weight = 70 000) and chlorobenzene (anhydrous, 99.8%) were purchased from Sigma-Aldrich. 1,3,5-Tris-(1-phenyl-1*H*-benzimidazol-2-yl)benzene (TPBi) and LiF were purchased from Jilin OLED Photoelectric Material Corporation. Poly(2,3-dihydrothieno-1,4-dioxin)-poly(styrenesulfonate) (PEDOT:PSS) (PVP Al 4083) was purchased from Heraeus. All chemicals were used as received.

2.2 Preparation of perovskite precursor solutions

The perovskite solutions were prepared by dissolving PABr, PEABr, CsBr and $PbBr_2$ with molar ratio of 0.135 : 0.045 : 0.15 : 0.165 in DMSO. $EDACl_2$ and NaBr were added to the precursor solution as additives, the concentration of Cs was kept at 0.15 M. The solutions were stirred for 2 h at room temperature for dissolution, then filtered through a 0.22 μm polytetrafluoroethylene (PTFE) filter before spin coating.

2.3 Device fabrication

Glass substrates with a 180 nm thickness precoated ITO were cleaned with detergents and deionized water by ultrasonic, then dried for 30 min at 120 °C. After that glass substrates were treated with UV ozone for 25 min. For the modified PEDOT:PSS, PSSNa was added to the PEDOT:PSS aqueous solution at a mass concentration of 100 mg mL^{-1}. After complete dissolution, the solution is then diluted by half. The pristine PEDOT:PSS layer was obtained by spin-coating the PEDOT:PSS solution at 4000 rpm for 30 s and annealed in ambient air at 150 °C for 30 min. For the PSSNa-modified PEDOT:PSS layer, the spin-coating speed was adjusted to 9000 rpm for 30 s, followed by annealing at 150 °C in ambient air for 30 minutes. Then, the substrates were transferred into a nitrogen-filled glove box after cooling. Poly-TPD was spin coated at 4000 rpm from chlorobenzene (CB) solution with a concentration of 6 mg mL^{-1} and annealed at 150 °C for 30 min, then PVK was spin coated at 4000 rpm from CB solution with a concentration of 4 mg mL^{-1} and annealed at 160 °C for 30 min. The perovskite films were spin coated at 3000 rpm for 60 s and annealed at 90 °C for 10 min. Finally, the devices were transferred to a vacuum chamber for the deposition of TPBi (40 nm), LiF (1 nm), and Al electrodes (100 nm). The active area of the devices was 8 mm^2, which was determined by the overlap area between the Al cathode and the ITO anode.

2.4 Characterizations

The ultraviolet-visible absorption spectra were measured with a Shimadzu UV-3600 UV-vis-NIR spectrophotometer. The photoluminescence (PL) spectra were recorded using a Horiba Fluoromax-4 spectrofluorometer with an excitation wavelength of 365 nm. Time-resolved photoluminescence (TRPL) spectra were measured with a Hamamatsu streak camera system which has an ultimate temporal resolution of 1 ps. The laser source was the Coherent Astrella-1K-F Ultrafast Ti:Sapphire Amplifier (<100 fs, 1 kHz). 360 nm pump pulses were generated from a Light Conversion TOPAS-C optical parametric amplifier. The PLQYs of the perovskite films were recorded by a commercialized PLQY measurement system from Ocean Optics with excitation from a 365 nm LED. The broadband femtosecond transient absorption (TA) measurements were performed by using the Ultrafast System HELIOS TA spectrometer. The laser source was the Coherent Astrella-1K-F Ultrafast Ti:Sapphire Amplifier (<100 fs, 1 kHz). The broadband probe pulses (350–550 nm) were generated by focusing a small portion of the fundamental 800 nm laser pulses into an CaF_2 plate. 360 nm pump pulses were generated from a Light Conversion TOPAS-C optical parametric amplifier. The scanning electron microscope (SEM) images were obtained by a Zeiss Sigma FESEM. Film thickness was tested with a profilometer (DektakXT, Bruker, Germany). The high-resolution transmission electron microscopy (HRTEM) images were obtained using a JEOL JEM-F200 at an accelerating voltage of 200 kV, and the samples were prepared by peeling off the as-fabricated films and dispersing them in chlorobenzene, then dropping them on a copper mesh and drying them in a vacuum. PeLEDs were tested on the side entrance port of the integration sphere, which collected the forward light emission in a N_2-filled glove box at room temperature. A fiber integrated sphere (FOIS-1) coupled with a PMA spectrometer (PMA-12, Hamamatsu) was used to characterize the emission light. The *J–V* curves were obtained using a source meter (Keithley 2400, Tektronix). The output data were summarized and calculated using a computer.

3 Results and discussion

The precursor solution was prepared by dissolving cesium bromide (CsBr), lead bromide ($PbBr_2$), phenylethylammonium bromide (PEABr) and propylammonium bromide (PABr) in dimethyl sulfoxide (DMSO). PEABr and PABr were introduced as spacer materials into $CsPbBr_3$ to construct pure-Br quasi-2D perovskite emissive layer (EML). Quasi-2D PeLEDs were fabricated using a multilayer device architecture of indium tin oxide (ITO, ~190 nm)/poly(2,3-dihydrothieno-1,4-dioxin)-poly (styrenesulfonate) (PEDOT:PSS, ~30 nm)/poly(4-butyltriphenylamine)/poly(9-vinylcarbazole) (poly-TPD/PVK, ~15 nm)/perovskite (~30 nm)/1,3,5-tris-(1-phenyl-1*H*-benzimidazol-2-yl) benzene (TPBi, ~40 nm)/lithium fluoride (LiF, ~1 nm)/aluminum (Al, ~100 nm). As shown in Fig. 1a and b, despite the relatively high spacer materials content (100% PABr + 20% PEABr), the electroluminescence (EL) emission peak of the PeLEDs remains in the sky-blue region (488 nm) due to the limitations of pure Br-based perovskites, with a device external quantum efficiency (EQE) of 5.2%. To further blue-shift the emission peak, the first additive $EDACl_2$ was introduced into the precursor solution at a specific mass concentration (mg mL^{-1}). With the addition of 1 mg mL^{-1} $EDACl_2$, the EL emission peak of the PeLEDs significantly blue-shifted from 488 nm to 479 nm. We attribute this spectral blue shift to two factors: the incorporation of Cl into the halogen sites of the perovskite lattice and the modification of the phase distribution in quasi-2D perovskites by the diammonium group of EDA^{2+}. However, as the $EDACl_2$ concentration continued to increase, no significant additional blue shift was observed in the emission spectra. Notably, when the concentration reached 3 mg mL^{-1}, a slight red shift of less than 1 nm emerged, accompanied by a marked decrease in the device's EQE. We attribute this to halogen ion saturation at this stoichiometric ratio, where additional Cl could not be effectively incorporated into the perovskite structure, while the deep-level defects induced by Cl reduced the radiative recombination efficiency. The performance of PeLEDs with varying $EDACl_2$ concentrations is shown in Fig. S1,† and the corresponding parameters are summarized in Table S1.† The optimized $EDACl_2$ concentration was determined to be 1 mg mL^{-1}, but the PeLEDs under this condition still did not achieve pure blue emission. To address this, a second additive NaBr was introduced. With the addition of NaBr, the EL emission peak of the devices further blue-shifted, reaching 474 nm at a NaBr content of 10%, although the EQE decreased to 3.3%. Further increasing the NaBr content resulted in a significant drop in device efficiency, accompanied by only a marginal blue shift in the emission spectrum (Fig. S2 and Table S2†). Through the

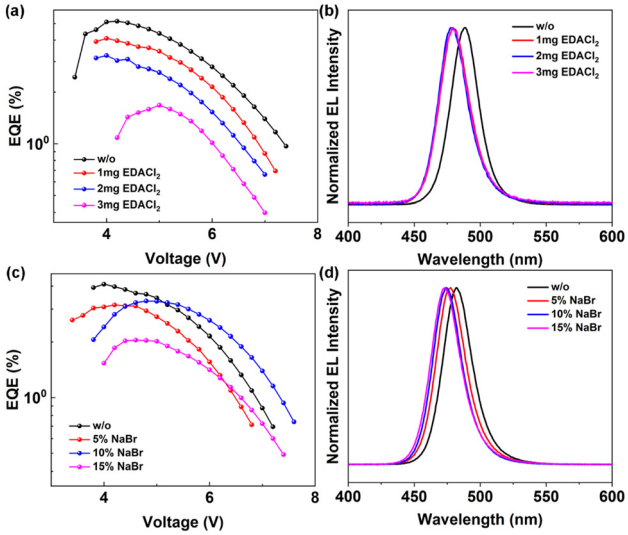

Fig. 1 Device performance of PeLEDs with different content of $EDACl_2$ and NaBr. (a, c) EQE *versus* voltage curves. (b, d) EL spectra at the voltage corresponding to the maximum EQEs.

co-optimization of $EDACl_2$ and NaBr, pure blue-emitting PeLEDs were successfully achieved. However, the physical mechanisms underlying the spectral blue shift and EQE reduction require further material characterization and investigation.

For quasi-2D perovskites, the variation in bandgap mainly stems from changes in the halogen sites and the phase distribution (n-value). The introduction of $EDACl_2$, which brings additional chlorine, predictably leads to a broadening of the bandgap. On the other hand, since the diamine groups of EDA^{2+} can coordinate with Pb ions, they may influence the original quasi-2D phase distribution. To investigate the impact of $EDACl_2$ on phase distribution, the perovskite films were analyzed using steady-state and transient absorption spectroscopy as characterization methods. From the absorption spectra (Fig. 2a), the control sample (labeled as w/o) exhibits two excitonic absorption peaks at ~400 nm and ~430 nm, corresponding to the n = 1 and n = 2 quasi-two-dimensional phases, respectively, along with a less steep absorption edge, corresponding to a series of high n-value phases. When $EDACl_2$ is introduced into the perovskite films (labeled as w/$EDACl_2$), the characteristic peak corresponding to the n = 1 phase almost disappears, while the peak for the n = 2 phase slightly blue-shifts. Both the characteristic peaks and the absorption edge show a noticeable blue shift, attributed to the introduction of chlorine. Notably, the slope of the absorption edge becomes significantly steeper, indicating that higher n-value phases are suppressed, and the overall phase distribution of the quasi-two-dimensional perovskite narrows. This can lead to a shift of radiative recombination centers towards phases with a wider bandgap, which is another main reason for the blue shift in the EL spectra. With the further introduction of NaBr into the perovskite films (labeled as w/$EDACl_2$ + NaBr), the phase distribution of the quasi-2D perovskite further narrows. The characteristic peak corresponding to the n = 2 phase almost disappears, leaving only the main characteristic peak at ~450 nm for the n = 3 phase, and the absorption edge shifts further blue, indicating a further shift in radiative recombination centers. HRTEM image reveal that the introduction of NaBr results in the formation of nanocrystals smaller than 10 nm in the quasi-two-dimensional perovskite film (Fig. S3†), suggesting that the transformation of narrow-bandgap high n-value and three-dimensional structures into wide-bandgap nanocrystal structures under the synergistic effect of $EDACl_2$ and NaBr is another reason for the overall bandgap broadening of the perovskite.[47]

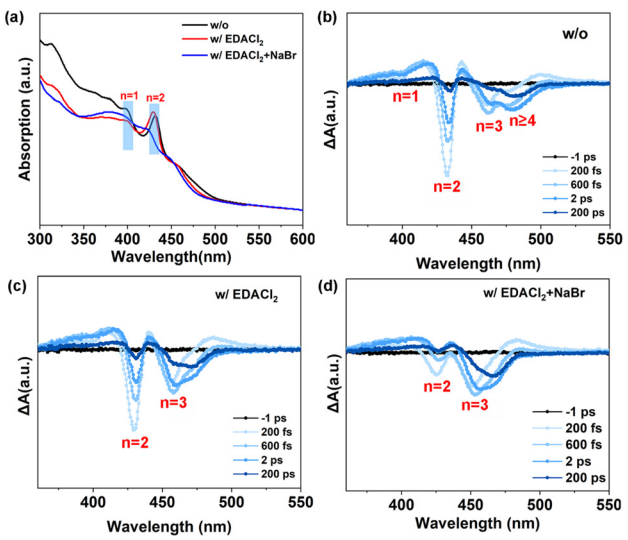

Fig. 2 Optical properties of quasi-2D perovskite films. (a) Absorption spectra and (b–d) TA spectra at different probe delay times for the films of w/o, w/$EDACl_2$, and w/$EDACl_2$ + NaBr, respectively, following excitation at 360 nm (100 fs, 1 kHz, 1.6 μJ cm^{-2}).

Fig. 2b–d show the TA spectra at different delay times for the three quasi-2D perovskite films. The w/o sample shows four bleach peaks located at 400 nm, 432 nm, 462 nm and 480 nm, corresponding to phases n = 1, 2, 3 and $n \geq 4$ respectively, which are consistent with the results of steady-state absorption spectra. After the introduction of $EDACl_2$ and NaBr, the bleach peak for n = 1 disappears, and the intensity of the n = 2 bleach peak significantly decreases, indicating that the low-dimensional phases have been significantly suppressed (Fig. 2c). All samples exhibit a broad bleach peak (Fig. 2b and c), corresponding to their emission centers, where the broad peak of the w/o is distinctly separate from the n = 3 bleach peak within the first 2 ps after excitation. However, after the introduction of $EDACl_2$ and NaBr, the broad peak gradually merges with the n = 3 bleach peak, indicating a gradual shift of radiative recombination centers towards intermediate phases such as n = 3 and n = 4. The shortened energy transfer path implies a more efficient and smoother energy transfer process. From the characterization results of steady-state and transient absorption spectroscopy, under the combined effect of $EDACl_2$ and NaBr, the phase distribution of the quasi-2D perovskite is centralized, with both low and high n-value phases suppressed, and medium n-value phases dominating. It is noteworthy that low n-value phases (n = 1, 2) have been reported to lead to non-radiative recombination in quasi-2D perovskites. The adjusted phase distribution not only shifts recombination centers towards wider bandgap phases but also effectively reduces non-radiative recombination centers, constructing a more efficient energy transfer pathway and enhancing the radiative recombination efficiency of the films. Considering that ligand materials are also important factors affecting the phase distribution of quasi-2D perovskites, the ratio of two ligand materials was readjusted, and their absorption and PL spectra were analyzed (Fig. S4†). As the content of PABr gradually increases, the PL peak of the perovskite film blue-shifts from 482 nm to 470 nm. However, when pure PABr is used as the ligand material, the PL intensity significantly decreases, and the peak symmetry worsens, showing obvious low-dimensional phase luminescence. From the absorption spectra, when the PABr content increases to 120%, the n = 1 and 2 phases significantly increase, and the absorption edge blue-shifts markedly, indicating that low-dimensional phases dominate, leading to more non-radiative recombination

centers. When the PEABr content is higher (100% and 120%), the absorption spectra show a characteristic peak at 314 nm corresponding to the Cs_4PbBr_6 phase, and the absorption edge is in the sky-blue region. Since Cs_4PbBr_6 hardly participates in radiative recombination luminescence, this phase distribution is unsuitable for the preparation of pure-blue quasi-2D perovskites. After comprehensive consideration, a ligand ratio of 100% PABr + 20% PEABr strikes a balance between pure-blue emission (474 nm) and strong PL intensity.

Based on the optimized phase distribution, the radiative recombination efficiency of perovskite films should have been effectively improved. However, the corresponding PeLEDs exhibit a decreasing trend in EQE. To investigate the reason, we conducted photoluminescence quantum yield (PLQY) and time-resolved photoluminescence (TRPL) measurements to explore the underlying mechanism (Fig. 4a and b). The PLQY for the three types of films—w/o, w/$EDACl_2$, and w/$EDACl_2$ + NaBr—were 66%, 55%, and 64%, respectively. The decrease in PLQY for the w/$EDACl_2$ film might be attributed to Cl-induced deep-level defects, while the introduction of NaBr reduced the non-radiative recombination centers caused by low-dimensional phases, leading to an increased PLQY.

TRPL decay profiles were fitted by a bi-exponential function, with detailed fitting parameters provided in Table S3.† The decay process is characterized by two distinct lifetime components: τ_1 (fast decay) and τ_2 (slow decay). According to previous work,[39] the slow decay component can be attributed to radiative recombination, while the fast component can be attributed to trap-assisted recombination. Based on the calculated average lifetime (τ_{avg}) and PLQY, we further calculated the radiative (k_{rad}) and non-radiative (k_{nonrad}) recombination rates for the perovskite films. Compared with w/o, although the introduction of $EDACl_2$ slightly reduced k_{nonrad} by suppressing non-radiative recombination from the n = 1 phase, k_{rad} also significantly decreased. On one hand, the introduced $EDACl_2$, as a surface ligand, has poor conductivity, leading to a decrease in the intrinsic carrier mobility of perovskite. On the other hand, the additional introduction of Cl in the halogen sites of perovskite not only brings deep-level defects, increasing the non-radiative recombination rate (which overlaps with the reduction of k_{nonrad} due to phase distribution regulation), but also affects the intrinsic properties of perovskite, both of which lead to a decrease in k_{rad}. After the introduction of NaBr, although k_{rad} remained almost unchanged, its stronger phase distribution regulation effect (significantly reducing the formation of low-dimensional phases, thereby suppressing non-radiative recombination centers) led to a significant reduction in k_{nonrad}, thus improving PLQY. From the film morphology observed by scanning electron microscopy (Fig. 3c), the introduction of $EDACl_2$ significantly reduced the large-sized particles in the film, while the introduction of NaBr significantly improved the crystallinity, with clear flaky quasi-2D phases and small-sized 3D phases visible.

From the optical characterization results of the thin films, although the k_{rad} decreased after the introduction of $EDACl_2$ and NaBr, the negative impact was further offset by the reduction in k_{nonrad}, ultimately resulting in a PLQY close to that of the w/o sample. Therefore, the decline in EQEs of the PeLEDs is likely due to structural defects in the device. PEDOT:PSS, widely used as a hole transport layer, has a significant issue with interfacial exciton quenching.[48] To address this problem, we introduced a poly-TPD/PVK layer as a spacer for quenching protection, while also considering conductivity and surface wettability. However, this introduces an additional barrier for hole transport (the HOMO levels of PEDOT:PSS, poly-TPD, and PVK are −5.0 eV, −5.2 eV, and −5.8 eV, respectively). Introducing PSSNa into PEDOT:PSS has been proven to be an effective strategy to lower the HOMO level and improve the surface morphology of the PEDOT:PSS layer, reducing exciton quenching. We modified the PEDOT:PSS layer and prepared PeLEDs for comparison. The device structure is shown in Fig. 4a, where the pristine PEDOT:PSS layer and the PSSNa-introduced PEDOT:PSS layer serve as hole injection layers, respectively, with the poly-TPD/PVK layer acting as a spacer and hole transport layer, and TPBi as the electron transport layer. Fig. 4b–f show the current density–luminance–voltage (J–L–V), external quantum efficiency–voltage (EQE–V), current efficiency–voltage (CE–V) characteristics, normalized electroluminescence (EL) spectra, and EL color coordinates of the PeLEDs. The performance of both PeLEDs is summarized in Table S4,† where the PeLED with introduced PSSNa exhibits a lower turn-on voltage, indicating improved energy level matching in the device. The maximum brightness and maximum EQE of the PeLED with the modified hole transport layer were enhanced, with the maximum EQE reaching 4.6% (Fig. 4b, c and Fig. S5†). Moreover, there was almost no significant change in the EL spectra, suggesting that the radiative recombination centers of the device remained unchanged. Notably, although we introduced a small amount of Cl, the EL spectra shows almost no change under continuously increasing operating voltages, maintaining a blue light emission at 474 nm even under an extreme high bias of 10.4 V. Furthermore, the

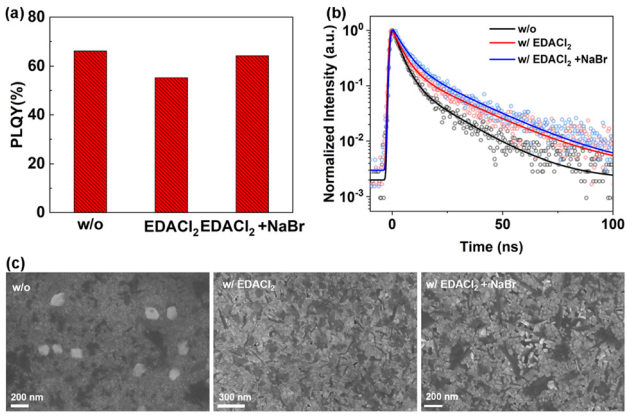

Fig. 3 Radiation mechanism and surface morphology analysis of quasi-2D perovskite films. (a) PLQYs excited using a 365 nm LED, and (b) photoluminescence decay at the emission peaks excited with 375 nm laser pulses (68.8 ps, 1 MHz, 10 nJ cm^{-2}) the films of w/o, w/$EDACl_2$, and w/$EDACl_2$ + NaBr, respectively. (c) SEM images of three kinds of films.

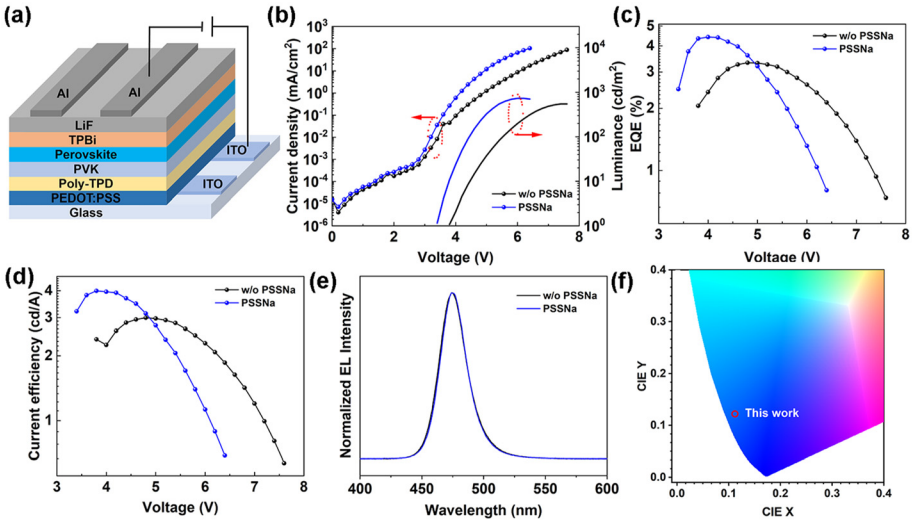

Fig. 4 Optimization of device performance by modified PEDOT:PSS hole transport layer. (a) Device structure diagram. (b) *J*–*L*–*V* characteristics. (c) EQE *versus* voltage curves. (d) Current efficiency *versus* voltage curves. (e) EL spectra at the voltage corresponding to the maximum EQEs. (f) CIE coordinates.

spectrum also remained stable during prolonged operation at fixed voltages (Fig. S6 and S7†). This is due to the saturation of halogen sites reducing the formation of halogen defects, and the relatively low Cl content. In contrast, we prepared a mixed Cl–Br quasi-2D PeLED without the introduction of $EDACl_2$ and NaBr, whose EL spectra showed a significant redshift with increasing bias voltage (Fig. S6†). Our dual-additive phase distribution regulation strategy provides a viable approach for the fabrication of color stable pure blue quasi-2D PeLEDs.

4 Conclusions

In this study, we successfully developed efficient and color-stable pure-blue perovskite light-emitting diodes (PeLEDs) through a dual-additive strategy that modulates phase distribution and manages chlorine incorporation in quasi-2D perovskites. By introducing $EDACl_2$ to suppress high-*n* phases and incorporate Cl for bandgap broadening, combined with NaBr to eliminate low-*n* non-radiative centers and promote small-sized nanocrystals, we optimized radiative recombination towards wide-bandgap phase distribution. This approach enabled spectrally stable pure-blue electroluminescence at 474 nm without compromising PLQY. Further engineering of the hole transport layer yielded a peak EQE of 4.6%, with spectral stability maintained under extreme bias up to 10.4 V. Our findings provide critical insights into phase and halide management for high-performance blue PeLEDs, advancing their potential in full-color displays and lighting technologies. This work underscores the importance of precise material engineering in overcoming the challenges associated with blue perovskite emitters, paving the way for future advancements in perovskite optoelectronics.

Author contributions

G. X. supervised the work and conceived the idea. P. P. fabricated devices and analyzed the data. P. P. performed UV-vis-NIR, PL, and PLQY measurements and analyzed the data. P. P., B. W., and Z. Z. performed TA measurements and analyzed the data. P. P. performed TRPL measurements and analyzed the data. P. P. and T. S. performed SEM and HRTEM measurements and analyzed the data. P. P. wrote the paper. G. X., Z. Z., B. W. and T. S. revised the paper. All authors read and commented on the paper.

Data availability

The data that support the findings of this study are available from the corresponding author upon reasonable request.

Conflicts of interest

There are no conflicts to declare.

Acknowledgements

The authors acknowledge the Science and Technology Development Fund, Macao SAR (file no. FDCT-0082/2021/A2, 0010/2022/AMJ, 0060/2023/RIA1, 0136/2022/A3, 006/2022/ALC, 0122/2024/AMJ, EF044/IAPME-HG/2022/MUST), UM's research fund (file no. MYRG2022-00241-IAPME, MYRG-GRG2023-00065-IAPME-UMDF, MYRG-CRG2022-00009-FHS), the research fund from Wuyi University (EF38/IAPME-XGC/2022/WYU), the Natural Science Foundation of China (61935017,

62175268, 62288102, 22405010), and the National Key Research and Development Program of China (2022YFE0206000).

References

1 Z.-K. Tan, R. S. Moghaddam, M. L. Lai, P. Docampo, R. Higler, F. Deschler, M. Price, A. Sadhanala, L. M. Pazos, D. Credgington, F. Hanusch, T. Bein, H. J. Snaith and R. H. Friend, *Nat. Nanotechnol.*, 2014, **9**, 687–692.
2 L. Dou, A. B. Wong, Y. Yu, M. Lai, N. Kornienko, S. W. Eaton, A. Fu, C. G. Bischak, J. Ma, T. Ding, N. S. Ginsberg, L.-W. Wang, A. P. Alivisatos and P. Yang, *Science*, 2015, **349**, 1518–1521.
3 M. Saliba, T. Matsui, J.-Y. Seo, K. Domanski, J.-P. Correa-Baena, M. K. Nazeeruddin, S. M. Zakeeruddin, W. Tress, A. Abate, A. Hagfeldt and M. Grätzel, *Energy Environ. Sci.*, 2016, **9**, 1989–1997.
4 S. D. Stranks and H. J. Snaith, *Nat. Nanotechnol.*, 2015, **10**, 391–402.
5 Y.-H. Kim, H. Cho, J. H. Heo, T.-S. Kim, N. Myoung, C.-L. Lee, S. H. Im and T.-W. Lee, *Adv. Mater.*, 2015, **27**, 1248–1254.
6 L. Protesescu, S. Yakunin, M. I. Bodnarchuk, F. Krieg, R. Caputo, C. H. Hendon, R. X. Yang, A. Walsh and M. V. Kovalenko, *Nano Lett.*, 2015, **15**, 3692–3696.
7 A. Kojima, K. Teshima, Y. Shirai and T. Miyasaka, *J. Am. Chem. Soc.*, 2009, **131**, 6050–6051.
8 H. Cho, S.-H. Jeong, M.-H. Park, Y.-H. Kim, C. Wolf, C.-L. Lee, J. H. Heo, A. Sadhanala, N. Myoung, S. Yoo, S. H. Im, R. H. Friend and T.-W. Lee, *Science*, 2015, **350**, 1222–1225.
9 Y. Cao, N. Wang, H. Tian, J. Guo, Y. Wei, H. Chen, Y. Miao, W. Zou, K. Pan, Y. He, H. Cao, Y. Ke, M. Xu, Y. Wang, M. Yang, K. Du, Z. Fu, D. Kong, D. Dai, Y. Jin, G. Li, H. Li, Q. Peng, J. Wang and W. Huang, *Nature*, 2018, **562**, 249–253.
10 X. Zhao and Z.-K. Tan, *Nat. Photonics*, 2020, **14**, 215–218.
11 Z. Chu, Q. Ye, Y. Zhao, F. Ma, Z. Yin, X. Zhang and J. You, *Adv. Mater.*, 2021, **33**, 2007169.
12 Y. Dong, Y.-K. Wang, F. Yuan, A. Johnston, Y. Liu, D. Ma, M.-J. Choi, B. Chen, M. Chekini, S.-W. Baek, L. K. Sagar, J. Fan, Y. Hou, M. Wu, S. Lee, B. Sun, S. Hoogland, R. Quintero-Bermudez, H. Ebe, P. Todorovic, F. Dinic, P. Li, H. T. Kung, M. I. Saidaminov, E. Kumacheva, E. Spiecker, L.-S. Liao, O. Voznyy, Z.-H. Lu and E. H. Sargent, *Nat. Nanotechnol.*, 2020, **15**, 668–674.
13 K. Lin, J. Xing, L. N. Quan, F. P. G. de Arquer, X. Gong, J. Lu, L. Xie, W. Zhao, D. Zhang, C. Yan, W. Li, X. Liu, Y. Lu, J. Kirman, E. H. Sargent, Q. Xiong and Z. Wei, *Nature*, 2018, **562**, 245–248.
14 Z. Liu, W. Qiu, X. Peng, G. Sun, X. Liu, D. Liu, Z. Li, F. He, C. Shen, Q. Gu, F. Ma, H.-L. Yip, L. Hou, Z. Qi and S.-J. Su, *Adv. Mater.*, 2021, **33**, 2103268.
15 D. Ma, K. Lin, Y. Dong, H. Choubisa, A. H. Proppe, D. Wu, Y.-K. Wang, B. Chen, P. Li, J. Z. Fan, F. Yuan, A. Johnston, Y. Liu, Y. Kang, Z.-H. Lu, Z. Wei and E. H. Sargent, *Nature*, 2021, **599**, 594–598.
16 M.-H. Park, J. Park, J. Lee, H. S. So, H. Kim, S.-H. Jeong, T.-H. Han, C. Wolf, H. Lee, S. Yoo and T.-W. Lee, *Adv. Funct. Mater.*, 2019, **29**, 1902017.
17 C. Sun, Y. Jiang, M. Cui, L. Qiao, J. Wei, Y. Huang, L. Zhang, T. He, S. Li, H.-Y. Hsu, C. Qin, R. Long and M. Yuan, *Nat. Commun.*, 2021, **12**, 2207.
18 W. Xu, Q. Hu, S. Bai, C. Bao, Y. Miao, Z. Yuan, T. Borzda, A. J. Barker, E. Tyukalova, Z. Hu, M. Kawecki, H. Wang, Z. Yan, X. Liu, X. Shi, K. Uvdal, M. Fahlman, W. Zhang, M. Duchamp, J.-M. Liu, A. Petrozza, J. Wang, L.-M. Liu, W. Huang and F. Gao, *Nat. Photonics*, 2019, **13**, 418–424.
19 B. Zhao, S. Bai, V. Kim, R. Lamboll, R. Shivanna, F. Auras, J. M. Richter, L. Yang, L. Dai, M. Alsari, X.-J. She, L. Liang, J. Zhang, S. Lilliu, P. Gao, H. J. Snaith, J. Wang, N. C. Greenham, R. H. Friend and D. Di, *Nat. Photonics*, 2018, **12**, 783–789.
20 L. Zhu, H. Cao, C. Xue, H. Zhang, M. Qin, J. Wang, K. Wen, Z. Fu, T. Jiang, L. Xu, Y. Zhang, Y. Cao, C. Tu, J. Zhang, D. Liu, G. Zhang, D. Kong, N. Fan, G. Li, C. Yi, Q. Peng, J. Chang, X. Lu, N. Wang, W. Huang and J. Wang, *Nat. Commun.*, 2021, **12**, 5081.
21 T. Chiba, Y. Hayashi, H. Ebe, K. Hoshi, J. Sato, S. Sato, Y.-J. Pu, S. Ohisa and J. Kido, *Nat. Photonics*, 2018, **12**, 681–687.
22 J. Jiang, Z. Chu, Z. Yin, J. Li, Y. Yang, J. Chen, J. Wu, J. You and X. Zhang, *Adv. Mater.*, 2022, **34**, 2204460.
23 K. Wang, Z.-Y. Lin, Z. Zhang, L. Jin, K. Ma, A. H. Coffey, H. R. Atapattu, Y. Gao, J. Y. Park, Z. Wei, B. P. Finkenauer, C. Zhu, X. Meng, S. N. Chowdhury, Z. Chen, T. Terlier, T.-H. Do, Y. Yao, K. R. Graham, A. Boltasseva, T.-F. Guo, L. Huang, H. Gao, B. M. Savoie and L. Dou, *Nat. Commun.*, 2023, **14**, 397.
24 Y.-C. Ye, Y.-Q. Li, X.-Y. Cai, W. Zhou, Y. Shen, K.-C. Shen, J.-K. Wang, X. Gao, I. S. Zhidkov and J.-X. Tang, *Adv. Funct. Mater.*, 2021, **31**, 2105813.
25 W. Bai, T. Xuan, H. Zhao, H. Dong, X. Cheng, L. Wang and R.-J. Xie, *Adv. Mater.*, 2023, **35**, 2302283.
26 S.-Q. Sun, J.-W. Tai, W. He, Y.-J. Yu, Z.-Q. Feng, Q. Sun, K.-N. Tong, K. Shi, B.-C. Liu, M. Zhu, G. Wei, J. Fan, Y.-M. Xie, L.-S. Liao and M.-K. Fung, *Adv. Mater.*, 2024, **36**, 2400421.
27 Z. Xing, G. Jin, Q. Du, P. Pang, T. Liu, Y. Shen, D. Zhang, B. Yu, Y. Liang, D. Yang, J. Tang, L. Wang, G. Xing, J. Chen and D. Ma, *Adv. Mater.*, 2024, **36**, 2406706.
28 Z. Ren, J. Yu, Z. Qin, J. Wang, J. Sun, C. C. S. Chan, S. Ding, K. Wang, R. Chen, K. S. Wong, X. Lu, W.-J. Yin and W. C. H. Choy, *Adv. Mater.*, 2021, **33**, 2005570.
29 F. Zhang, Y. Yang, Y. Gao, D. Wang, W. Dong, P. Lu, X. Wang, M. Lu, Y. Wu, P. Chen, J. Hu, X. Yang, D. Zhou, D. Liu, L. Xu, B. Dong, Z. Wu, Y. Zhang, H. Song and X. Bai, *Nano Lett.*, 2024, **24**, 1268–1276.
30 Y.-C. Ye, Y. Shen, W. Zhou, S.-C. Feng, J.-Y. Wang, Y.-Q. Li and J.-X. Tang, *Adv. Funct. Mater.*, 2023, **33**, 2307818.

31 L. Wang, Z.-H. Su, Y. Shen, S.-C. Feng, F.-M. Xie, K. Zhang, K.-F. Meng, X. Gao, J.-X. Tang and Y.-Q. Li, *Adv. Funct. Mater.*, 2024, **34**, 2401297.
32 S. Liu, Z. Guo, X. Wu, X. Liu, Z. Huang, L. Li, J. Zhang, H. Zhou, L.-D. Sun and C.-H. Yan, *Adv. Mater.*, 2023, **35**, 2208078.
33 V. K. Ravi, G. B. Markad and A. Nag, *ACS Energy Lett.*, 2016, **1**, 665–671.
34 R. E. Brandt, V. Stevanović, D. S. Ginley and T. Buonassisi, *MRS Commun.*, 2015, **5**, 265–275.
35 A. Sadhanala, S. Ahmad, B. Zhao, N. Giesbrecht, P. M. Pearce, F. Deschler, R. L. Z. Hoye, K. C. Gödel, T. Bein, P. Docampo, S. E. Dutton, M. F. L. De Volder and R. H. Friend, *Nano Lett.*, 2015, **15**, 6095–6101.
36 P. Vashishtha, M. Ng, S. B. Shivarudraiah and J. E. Halpert, *Chem. Mater.*, 2019, **31**, 83–89.
37 Y. Shen, K.-C. Shen, Y.-Q. Li, M. Guo, J. Wang, Y. Ye, F.-M. Xie, H. Ren, X. Gao, F. Song and J.-X. Tang, *Adv. Funct. Mater.*, 2021, **31**, 2006736.
38 Q. Zhang, D. Zhang, Z. Liao, Y. B. Cao, M. Kumar, S. Poddar, J. Han, Y. Hu, H. Lv, X. Mo, A. K. Srivastava and Z. Fan, *Adv. Mater.*, 2024, 2405418.
39 P. Pang, G. Jin, C. Liang, B. Wang, W. Xiang, D. Zhang, J. Xu, W. Hong, Z. Xiao, L. Wang, G. Xing, J. Chen and D. Ma, *ACS Nano*, 2020, **14**, 11420–11430.
40 Z. Li, Z. Chen, Y. Yang, Q. Xue, H.-L. Yip and Y. Cao, *Nat. Commun.*, 2019, **10**, 1027.
41 M. Zeng, D. Chen, J. Wang, D. Li, G. Xie, J. Ou, L. Wang and J. Wang, *ACS Appl. Mater. Interfaces*, 2023, **15**, 36620–36627.
42 Y. Tong, X. Bi, S. Xu, H. Min, L. Cheng, Z. Kuang, L. Yuan, F. Zhou, Y. Chu, L. Xu, L. Zhu, N. Zhao, N. Wang, W. Huang and J. Wang, *Adv. Mater.*, 2023, **35**, 2207111.
43 P. Xia, Y. Lu, H. Yu, Y. Li, W. Zhu, X. Xu, W. Zhang, J. Qian, W. Shen, L. Liu, L. Deng and S. Chen, *Nanoscale*, 2019, **11**, 20847–20856.
44 S. Yuan, T. Fang, B. Han, Q. Shan, C. Wei, X. Zheng, X. Li, B. Xu and H. Zeng, *Adv. Funct. Mater.*, 2024, **34**, 2316206.
45 D. P. Nenon, K. Pressler, J. Kang, B. A. Koscher, J. H. Olshansky, W. T. Osowiecki, M. A. Koc, L.-W. Wang and A. P. Alivisatos, *J. Am. Chem. Soc.*, 2018, **140**, 17760–17772.
46 R. Lai and K. Wu, *J. Chem. Phys.*, 2019, **151**, 194701.
47 P. Pang, Z. Xing, J. Xia, B. Wang, Z. Zhang, J. Guo, T. Liu, B. He, J. Chen, S. Chen and G. Xing, *Adv. Opt. Mater.*, 2022, **10**, 2201112.
48 X. Zheng, C. Wei, S. Yuan, D. Zhang, X. Li, X. Luo, W. Lu, B. Xu and J. Huang, *Appl. Surf. Sci.*, 2024, **655**, 159643.